DOI: 10.13009/EUCASS2022-4370
9TH EUROPEAN CONFERENCE FOR AERONAUTICS AND SPACE SCIENCES (EUCASS)

REST HF10 test case: Simulation of combustion instabilities induced by flow rate modulations with diffuse interface modelling

Aurélie Nicole and Luc-Henry Dorey**
** DMPE, ONERA, Université Paris Saclay, F-91123 Palaiseau, France, aurelie.nicole@onera.fr*

Abstract
Within the framework of studies on high-frequency combustion instabilities, the REST group has confronted its teams on a numerical case investigating the influence of inflow oscillations on these HF instabilities. ONERA has computed this case with an U-RANS approach, using a diffuse interface model and a pseudo-evaporation reaction to deal with the transcritical injection of oxygen. ONERA simulated the steady state and the modulations of the oxygen and methane inflow. The dense core is deformed as well as the flame front. The effect is greater at 1 kHz than at 5 kHz and the modulation of oxygen inflow has more influence than methane one.

1 Introduction

Since the beginning of the space race, high-frequency instabilities (HF) have been one of the major issues of liquid rocket engines development and qualification [1]. Their consequences are often serious as they can lead to engine destruction [2][3]. Competition from new private players is pushing manufacturers to reduce the development and implementation costs of their rockets. Recent innovations tend to increase the risk of instability in the operating regime of the engines, like the use of methane instead of hydrogen [4][5]. REST group (Rocket Engine Stability iniTiative), a French–German research cooperation, has worked on the HF issues. The group's objective is to provide models and data for predictive engineering tools to assist in the design of stable combustion chambers and to assess engine stability margins. Confidence in numerical tools has greatly increased over the last 20 years. Thereby, computational fluid dynamics (CFD) studies are carried out in order to better understand some phenomena that cannot yet be explored on experimental test benches. In this framework, a modelling test case was proposed to study the HF combustion instabilities driven by the propellants inflow rate oscillations. The computational domain represents part of an engine chamber consisting of a hexagonal domain with periodic boundary conditions and a Lox/Methane coaxial injection element. Conditions are similar to combustion chamber ones: the chamber pressure is equal to 100 bar, the injection is transcritical and the mixture ratio is nearby stoichiometry. ONERA has computed this case with an unsteady Reynolds-averaged Navier–Stokes approach (U-RANS), using CEDRE, the ONERA in-house CFD tool [6]. In a first part, the test case is presented (section 2) and then, the numerical and physical models are detailed (section 3). After examining the average flow (section 4), the different modulated cases are simulated and compared (section 5).

2 Presentation of the HF10 test case

2.1 Geometry

The HF10 test case investigates the high-frequency combustion instabilities driven by the propellants inflow rate oscillations. The particularity of this case is that it is a purely numerical test case. It allows an easy comparison between the different numerical approaches with various codes. The objective is to compare these methods and codes on a representative application of the combustion dynamics of rocket engines. The injector geometry was designed within the framework of the "Sonderforschungsbereich Transregio 40" funded by the "Deutsche Forschungsgemeinschaft" (DFG). It is intended to be adapted to both the LOx-CH_4 and the LOx-H_2 ergols. For the HF10 case, the simulation is carried out with LOx-CH_4 propellants, in the supercritical regime (100 bar) with a mix ratio of 3.4 and a momentum flux ratio equal to 4.34.

DOI: 10.13009/EUCASS2022-4370

The calculation area shown in Figure 1, includes an injector (Figure 1b) and a hexahedral part of the combustion chamber (Figure 1a). This hexahedral chamber part has a side length of 10.17 mm. The three pairs of opposing faces are connected by periodic conditions to allow freedom of movement of the flame. This type of configuration allows to represent an injector in the middle of its neighbours in a full engine. The flame is not isolated, but is surrounded by a large number of other flames. Table 1 shows the dimensions of the injector.

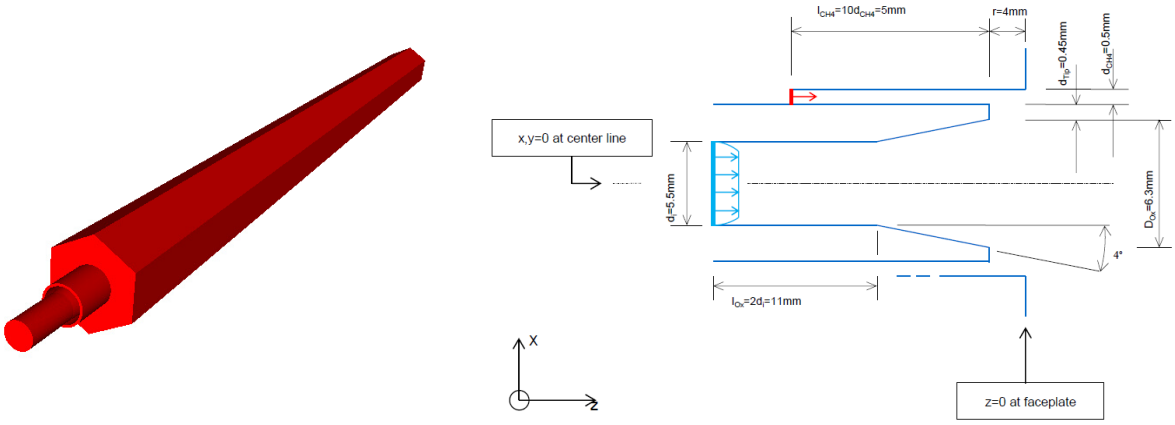

a) General view of the HF10 configuration

b) Injector

Figure 1: Scheme of the configuration

Description	Symbol	Unity	Value
Inner LOx post diameter	d_j	mm	5.5
LOx post exit diameter	D_{Ox}	mm	6.3
Outer Lox post diameter	$D_{Ox} + 2d_{Tip}$	mm	7.2
Outer diameter CH_4 sleeve	$d_{Fu} = D_{Ox} + 2d_{Tip} + 2d_{CH4}$	mm	8.2
CH_4 post diameter	d_{CH4}	mm	0.5
Recess	r	mm	4.0
Lox post lip thickness	d_{Tip}	mm	0.45
Taper angle	α	°	8.0

Table 1: injector characteristics

2.2 Boundary conditions

A scheme of the numerical setup and boundary conditions are presented in Figure 2. For the inlet conditions, the mass flow rate and temperature are imposed. This concerns the pitot lox inlet (green) and the methane injection line (blue). They are non-reflecting conditions and the velocity profile follows a 1/7 power law velocity profile $\left(U = U_0\left(1 - \frac{r}{R_0}\right)^{1/7}\right)$ in order to approximate fully developed turbulent flow conditions. The characteristic scale for the turbulent length is one third of the characteristic diameter and the turbulence level is set at 5%. The detail of the inlet conditions is given in Table 2.

For the exit (Red), the pressure is imposed at 100 bar and it is also a non-reflecting boundary conditions. Concerning the walls (black), it is no slipping and adiabatic walls. The pink dotted line represents the periodic condition and the pairing of the periodic faces is given in the right side of Figure 2.

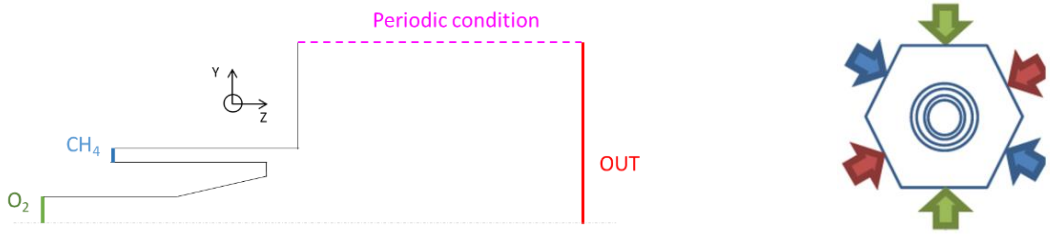

Figure 2: Boundary conditions (left) and pairwise periodic boundary conditions (right)

DOI: 10.13009/EUCASS2022-4370

		Oxygen	Methane
Mass flow rate	$kg.s^{-1}$	0.46	0.136
T	K	100	231
ρ	$kg.m^{-3}$	1116	149.4
U	$m.s^{-1}$	17.4	75.3
l	mm	$\frac{D_{ox}}{3} = 1.83$	$\frac{d_{ox} - d_i}{6} = 0.17$
τ	%	5	5
k	$m^2.s^{-2}$	1.13	21.25
ε	$J.kg^{-1}.s^{-1}$	107.5	96557.9
ω	s^{-1}	95.2	4544.5

Table 2: inlet conditions

2.3 Propellant features

Figure 3a (respectively Figure 3b) shows the evolution of density as a function of temperature for oxygen (respectively methane) at a pressure of 100 bar. The former is injected in liquid form before becoming supercritical, while the latter is injected in supercritical condition. The injection temperature is indicated by a red arrow on both graphs.

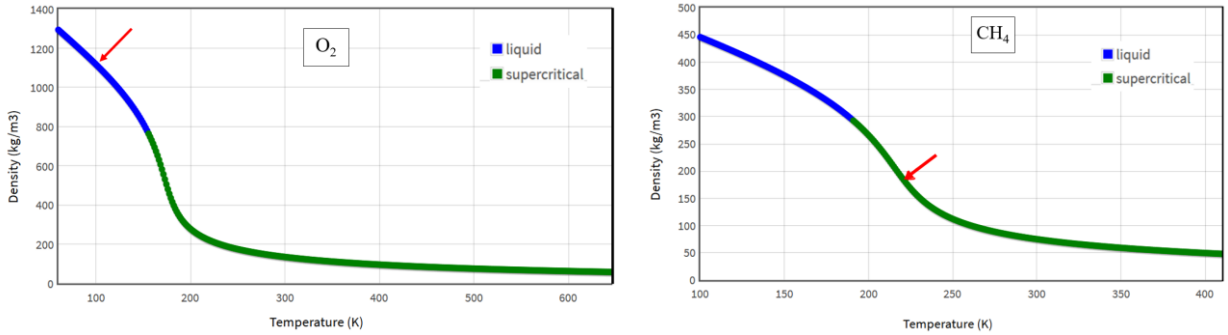

a) Oxygen density b) Methane density

Figure 3: Density versus temperature at 100 bar

Oxygen will therefore be considered in two forms: a dense form for the liquid injection part and a light form that will burn with the methane. The models used to treat these two oxygen phases will be explained in following .

3 Numerical and physical models

3.1 Turbulence model

A two-equation RANS model (k-SST Menter model [7]) is used for this simulation with linear Boussinesq closure assumptions. The first variable k is the turbulent kinetic energy and ω is the specific dissipation rate. This model was chosen because it is a hybrid model combining the Wilcox k-ω model and the k-ε model. A mixing function activates the Wilcox model near the walls and the k-ε model in the free flow. This ensures that the appropriate model is used throughout the flow field. Indeed, the k-ω model is suitable for simulating the flow in the viscous sublayer, while the strength of the k-ε model is a correct prediction of the flow behaviour in the regions away from the wall. The constants of the model have classical values except for the turbulent Prandtl number and turbulent Schmidt number are equal de 0.7 in accordance with [8]. The turbulence level was imposed at 5% and the turbulent characteristic scale is one third of the characteristic diameter.

3.2 Spatial discretization and time integration

For the spatial discretisation, the second order is used with a multi-slope method and a hybrid limiter. The set of variables interpolated to the faces for the evaluation of the numerical convective fluxes is a combination (P, U, T, ρU, Z) which is the most robust choice especially for configurations with high-density ratios as it is the case for the present configuration. P is for the pressure, T, the temperature, U the velocity, ρ the density and Z the scalars of the turbulence model. In the multi-slope method, the slope of each face contributes to the calculation of the face interpolations [9]. The hybrid limiter is a weighting between the Superbee limiter and a third order limiter for regular solutions. The numerical fluxes that approximate the convective fluxes at the mesh faces from the conserved quantities evaluated on both sides of the faces, are assessed by the HLLC (Harten-Lax-van Leer-Contact) methods introduced by Toro [10].These methods are quite robust and efficient but a bit diffusive. For this computation, concerning the spatial

DOI: 10.13009/EUCASS2022-4370

discretization which interpolates the physical fields at the faces between the cells for the calculation of the fluxes, order 2 has been chosen and the gradient is calculated by the unweighted least squares method from the mesh averages in the neighbouring cells. The time step is 5.10-7s with a CFL of the order of 1. A local time step is used, especially for the start-up phase of the calculation. The method for solving the implicit linear system is the GMRES method [11].

3.3 Mesh

A mesh convergence was performed with five grids. The first one is a coarse mesh which allowed the dense phase to be set up and the flame to be initiated. The solution was then projected onto increasingly finer meshes. The mesh is refined according to the areas of interest of the flame and the dense core. For the two first coarse meshes, only tetrahedron elements are used and then, prisms elements are used near the wall and tetrahedrons elsewhere. The final mesh chosen allowed the calculation to be sufficiently accurate and the output to be fast. This choice is determined by examining the influence of the mesh size on the length of the flame, its opening and the length of the dense core. It contains 11M elements and 2.3M nodes. The injector lips are meshed by 10 elements.

3.4 Combustion

For coaxial and swirl simulation, the same combustion formalism is used, namely the MRE (relaxation to equilibrium) model. This combustion model has been described in detail in the thesis of C. Le Touze [12]. It is a turbulent combustion model used for cases where the chemistry is infinitely fast (Da≫1). Da is the Damköhler number, it compares the turbulent time and the chemical time: $Da = \frac{\tau_{turbulent}}{\tau_{Chemical}}$. The chemical kinetics are not solved and the species reaction rates are driven by a turbulent mixing time. The Spalding [13] and Magnussen [14] models (EBU model: Eddy Break UP) and more recently Schmitt model [15] are based on the same principle. However, whereas these classical EBU models have reaction rates limited by the disappearance of the reactants from the overall reaction, for the MRE model, they are restricted by the local thermodynamic equilibrium which takes into account radical species. This leads to much more realistic combustion temperatures than with the EBU models. The average source term of a species *i* is written:

$$\overline{\dot{\omega}_i} = \rho\, min(C f_T, f_{max})\left(Y_{i,eq} - Y_i\right) H\left(T - T_{inf}\right), \quad i \epsilon \mathcal{R}$$

Where $\mathcal{R}$ is the set of chemical species involved in the calculation of the chemical equilibrium. This includes the reactants, the combustion products of the overall reaction, but also the radical species. In this expression, C is a reaction constant which is similar to the EBU model constant but which is not universal. The Heaviside function *H* can be used to cancel out the reaction rates if the temperature is below an ignition temperature T_{inf}. It is also possible to limit the reaction rate by a maximum frequency f_{max}. The equilibrium mass fractions $Y_{i,eq}$ are obtained at each iteration by a chemical equilibrium calculation based on the pseudo-reaction method or by tabulation at the beginning of the calculation. In the present simulation, the tabulation option was selected. Concerning f_T, the turbulent frequency, it is calculated by: $f_T = \frac{\varepsilon}{k}$.

In order to select the species of interest for the O_2/CH_4, combustion, a thermochemical equilibrium calculation is performed with the Cantera thermochemistry code [16] using the GRI-Mech 3.0 scheme [17]. This mechanism is an optimized mechanism designed to model natural gas combustion, including NO formation and reburn chemistry. It contains 325 reactions and 53 species. The predominant species appear to be CH_4, O_2, H_2O, CO_2, CO, H_2, OH, O and H. Their evolutions according mixture fraction is given by Figure 4, where mixture fraction is defined by: $Z = \frac{sY_F - Y_O + 1}{s+1} = \frac{1}{1+Rm}$ where s is the stoichiometry (s=4).

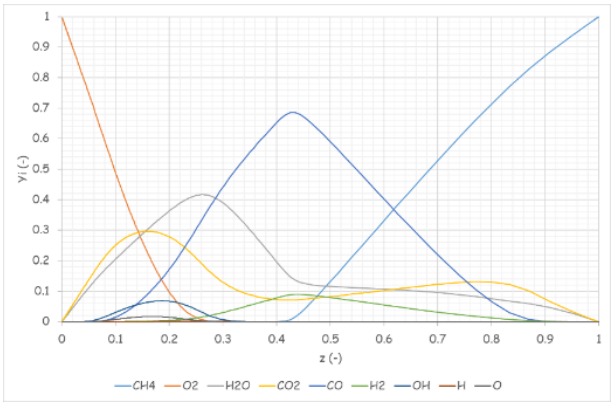

a) Mass fraction

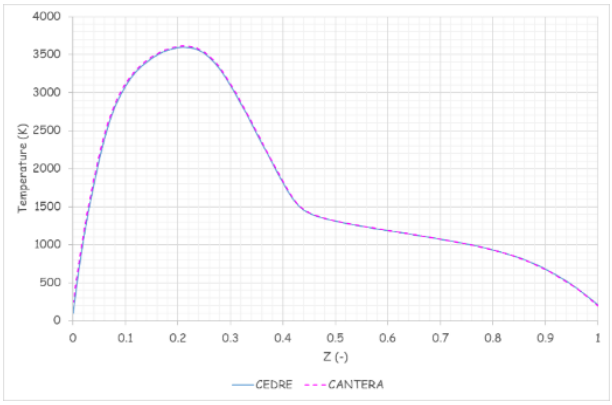

b) Temperature (CEDRE and Cantera results)

Figure 4. Mass fraction and temperature evolution according mixture fraction

DOI: 10.13009/EUCASS2022-4370

The MRE model is based on equilibrium tables. The equilibrium temperature is compared in Figure 4b with Cantera result. The comparison of the mass fractions (not represented here) shows that the OH mass fraction is slightly overestimated in the area close to stoichiometry.

3.5 Thermodynamic models

Two types of thermodynamics are used for these computations: ideal gas thermodynamics and real gas thermodynamics. The real gas state law is a cubic state law [18]. It takes into account the repulsive and attractive effects between the molecules. Its general form is:

$$P = \sum_i \frac{Y_i}{M_i} \frac{RT}{v-b} - \frac{a(T)}{v^2 + ubv + wb^2}$$

Where b is the covolume, $a(T)$ the cohesive pressure and u and w shape parameters. The covolume represents the minimum mass volume accessible to the mixture. For cubic state laws, ideal mixing is not assumed. The average properties of the fluid are calculated globally over all species of the same type from Van der Waals mixing laws. The parameters of species b_i and $a_i(T)$ are fixed in order to find the critical pressures and temperatures of the pure species. The determination of the cohesive pressure is completed by a temperature dependence following Soave's law completed by C^2 [19]:

$$\alpha(T_i^*) = \begin{cases} \left(1 + S_i\left(1 - \sqrt{T_i^*}\right)\right)^2, \forall T_i^* \leq 1, \\ \left(1 + \tanh\left[S_i\left(1 - \sqrt{T_i^*}\right)\right]\right)^2, \forall T_i^* > 1 \end{cases} \quad \text{with } S_i = 0.480 + 1.574\omega - 0.175\omega^2$$

When injected at low temperatures, the Soave-Redlich-Kwong model reproduces fewer non-linearities in the transcritical zone than other models and it allows to recover more stable densities.

Two phases are used:

- A "light" phase with the following species: CH_4, O_2, H_2O, CO_2, CO, H_2, O, H and OH ;
- A "dense" phase containing only dense oxygen.

In the light phase, the gases are considered perfect. And the dense oxygen follows the cubic law of state (Soave completed C^2). For the dense phase, the mean shear viscosity and the mean thermal conductivity are evaluated according to the assumptions made by Ely-Hanley [20].

3.6 Transcritical modelling

In order to switch from the dense oxygen to its light form, the TPS model (Supercritical Phase Transfer Model) is used. This model is detailed in reference [21]. When oxygen is injected at subcritical pressure $\left(P < P_c^{O_2} = 50.428\ bar\right)$, the liquid phase exists at temperatures below the saturation temperature and vaporises at higher temperatures. When the injection pressure is higher than the critical pressure, the oxygen is in a critical state and changes from the dense state at low temperatures to a light state at high temperatures continuously. Nevertheless, there are still strong variations in the density of the supercritical fluid in the area extending the saturation curve, which can be linked to a pseudo-evaporation curve. Thus, transcritical injection conditions exist when cold injected propellants at supercritical pressures, which then heat up through combustion, pass through this pseudo-evaporation zone (transcritical transition or dense-dilute transition). While the subcritical regime is characterised by a jet atomisation in fibre-type elements and then droplets where the surface tension force plays an important role, in the supercritical regime, the pseudo-evaporation transition is dominated by diffusion phenomena. To treat the pseudo-evaporation of oxygen, a pseudo-chemical reaction is introduced to describe the mass exchange: $(O_2)_d \leftrightarrows (O_2)_l$

The index d is relative to the dense phase and the index l to the light phase. An Arrhenius law is associated to this equation, using an equilibrium constant K_* of the form:

$$K_* = \left(\frac{T}{T_{ref}}\right)^{2\beta}$$

The parameter β is to be adjusted according to the simulation conditions. Moreover, we imposed that the dense phase cannot have a temperature higher than 140 K. And above this temperature, the oxygen is necessarily "light" oxygen.

DOI: 10.13009/EUCASS2022-4370

4 Steady state solution

Figure 5 gives the temperature in the plane Y=0 and an iso-surface of density, which represents the dense core. Concerning the temperature fiels, the flame opens abruptly at the outlet of the injector and then closes, forming a kind of bump due to the confinement of the flame. The dense core is quite long and has an elongated cone shape.

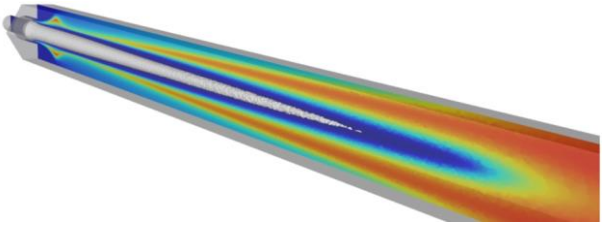

Figure 5: Temperature field in Y=0 and an iso-surface of density

This simulation highlighted a particularity of supercritical flows, namely the sudden expansion of the flame at the chamber entrance as shown in Figure 26. This figure shows the mass heat field at constant pressure at the top and the temperature field at the bottom in the X=0 cutting plane. Thus, from 5 mm to 12.5 mm, the flame opens abruptly and then resumes a classical evolution from 20 mm (Figure 6).

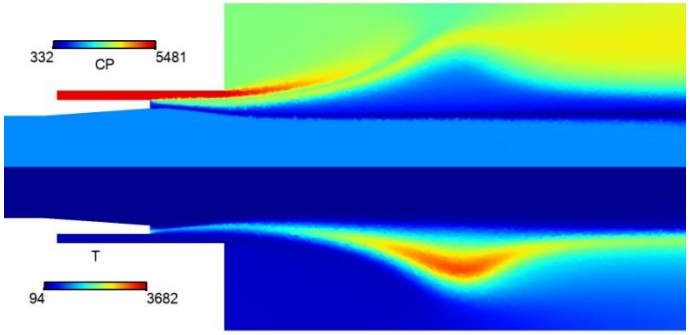

Figure 6: Field at the chamber entrance of constant pressure (top) and temperature (bottom) mass heat field (cut X=0)

While flame confinement could explain this shape, other phenomena also come into play as shown in reference [22]. A peak appears in the specific heat field at constant pressure in the region surrounding the dense jet. In this region, the heat transfer to the cryogenic oxygen does not significantly increase its temperature but simply increases its volume. This behaviour confirms a behaviour similar to pseudo-evaporation. The shape of the inlet flame is therefore due to this phenomenon combined with the confinement of the flame. The same calculation would have to be done with oxygen as a perfect gas to be completely sure.

Concerning the velocity, Figure 7 gives some cross-sections of the longitudinal one.

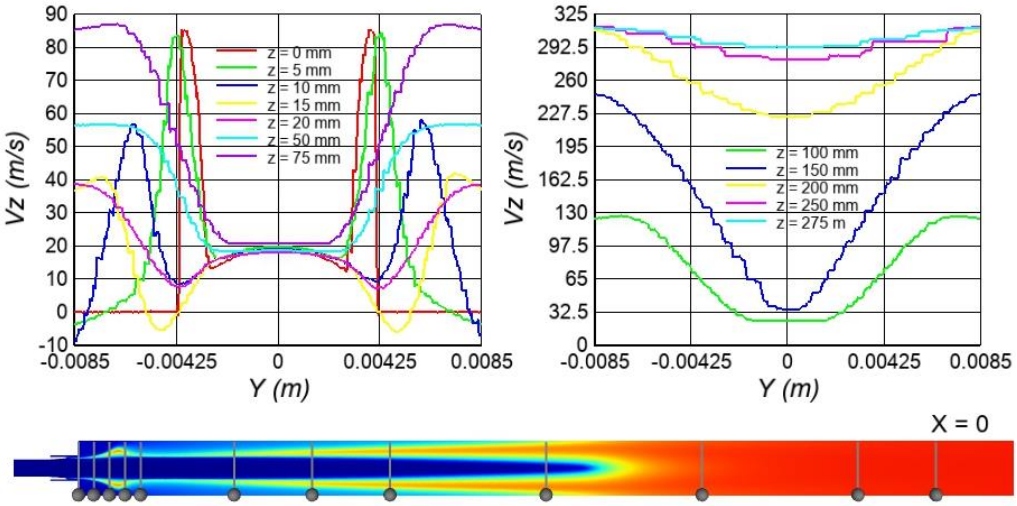

Figure 7: Transverse section of the longitudinal velocity Vz

DOI: 10.13009/EUCASS2022-4370

At the chamber inlet, this transverse velocity profile shows two peaks corresponding to the methane jets. These peaks gradually diverge while decreasing in amplitude as the distance from the injection plate increases (Z=0 to 15 mm), typical behaviour of a jet that opens up little by little, then from Z=20 mm, the jet sticks to the periodicity conditions. The velocity at the centre is lower, the dense core progresses more slowly in the chamber than the gas stream. A counter-current can even appear at Z=15 mm which corresponds to the temperature bump.

5 Mass flow excitation

The objective of this test case is to evaluate the influence of flow modulations on combustion in the context of high frequency combustion instabilities. Three modulation cases have been proposed:

- Excitation of the O_2 inlet at 1 kHz frequency: Modulation of the oxygen mass flow with a sinusoidal excitation of ±10% imposed directly on the boundary condition with a frequency of 1 kHz.
- Excitation of O_2 inlet at 5 kHz frequency: Modulation of O2 mass flow with ±10% sinusoidal excitation imposed directly on the boundary condition with a frequency of 5 kHz.
- Excitation of CH_4 inlet at 5 kHz frequency: Modulation of methane mass flow with ±10% sinusoidal excitation imposed directly on the boundary condition at 5 kHz frequency.

ONERA simulated the all three cases. To impose the flow fluctuation as well as the heterogeneous velocity condition, a specific condition is constructed.

5.1 Oxygen mass flow excitation at 1 kHz

At this frequency, a deformation of the dense core and temperature field appears as shown in Figure 8 and is easily analysed. Thus, the dense jet is wavy and shows about 5 structures. These waves appear every millisecond in coherence with the excitation frequency of the flow line. The length of the dense core is about 140 mm and the y-axis velocity is about 25 m/s. Each ripple is therefore about 25 mm apart, so the dense core may contain 5-6 ripples as shown in Figure 8. In addition, pockets of dense oxygen are intermittently shed as a liquid core beat is observed.

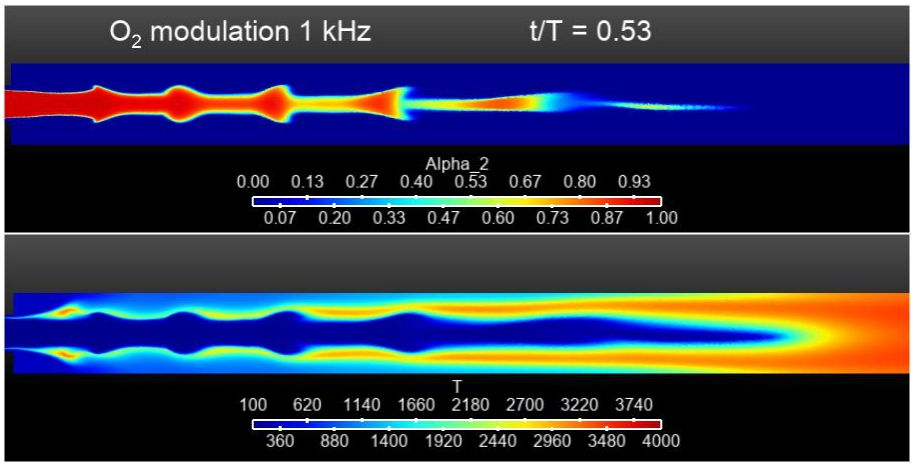

Figure 8: Instantaneous field of temperature and mass fraction of dense O_2 in the plane X=0

A deformation of the dense jet can also be seen. As shown in Figure 9, close to the injection plane, an arrow-like structure pointing towards the outlet (1) appears at Z 6.5m. The dense jet is strongly confined in the chamber. When the flow oscillation generates a ripple on the pseudo dense core surface, it can only develop from Z 6.5m due to the strong recirculation at the chamber inlet. Its shape is pinched and takes the form of an arrow pointing towards the chamber exit. In addition, as the temperature bump passes, recirculation can also form at the corrugation of the dense core as shown in Figure 10. The dense core acts as a wall for the hot gases to bounce off. These recirculations accentuate the deformation of the structures on the pseudo-interface. Then, these structures move towards the exit of the chamber while their shape evolves towards a more and more round structure (2) to then tend towards an arrow pointing towards the entrance (3). This is because the dense jet at the periphery is entrained faster than its centre by the surrounding gas flow. Eventually, the dense jet degrades due to mixing and a pocket eventually breaks away (4). This leads to a shortening of the liquid core length (Figure 11). The liquid jet is more compact and its length is divided by 2.

DOI: 10.13009/EUCASS2022-4370

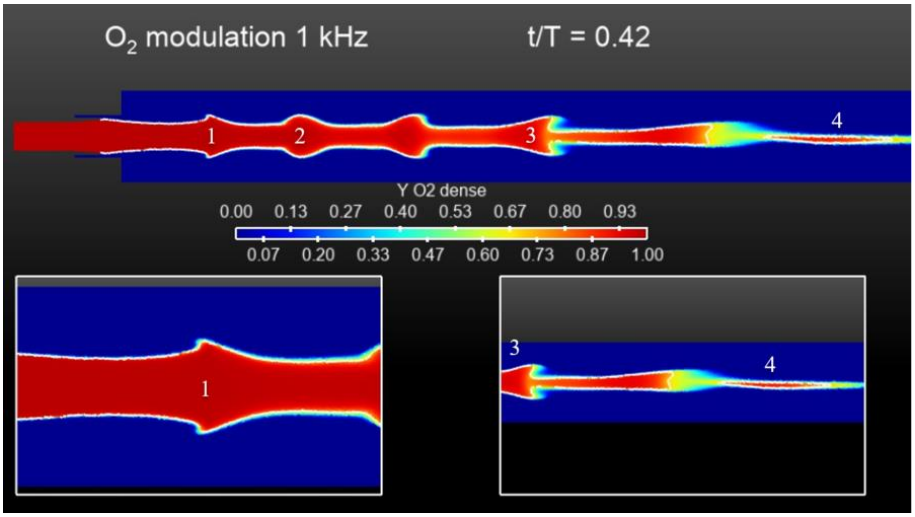

Figure 9: Deformation of the dense jet structure by O_2 inflow modulation at 1 kHz

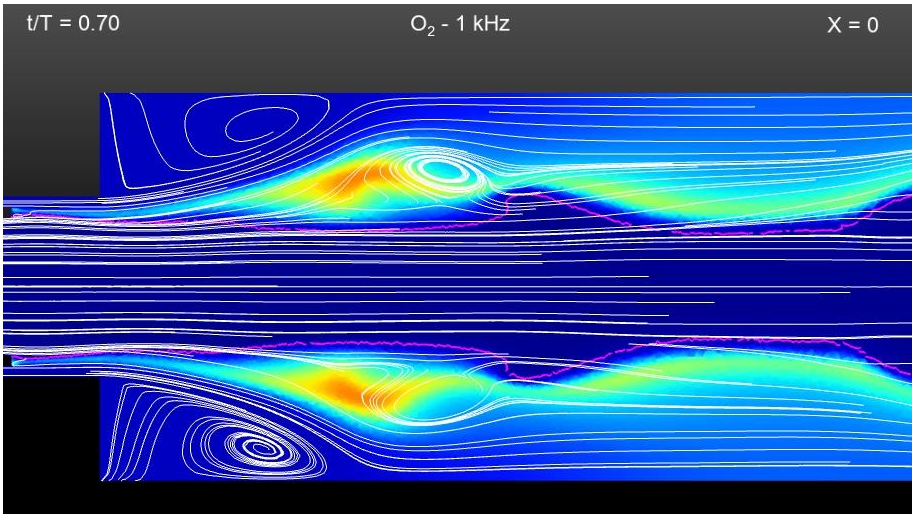

Figure 10: Streamline, temperature field and iso-contour of dense O_2 mass fraction in the X=0 plane (Zoom of the injection zone)

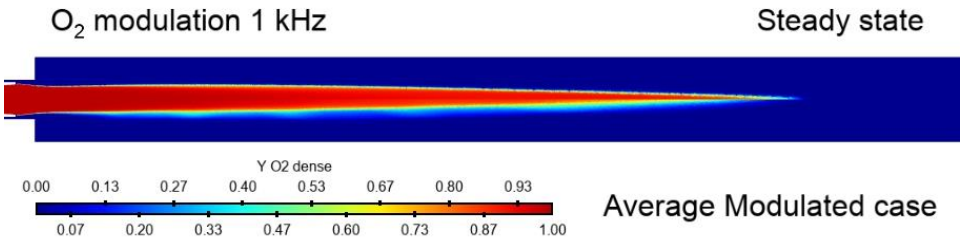

Figure 11: Comparison of the average dense O2 mass fraction fields for the steady state (top) and the modulated case (bottom) at 1 kHz

The flame is wrinkled by the corrugations of the dense core but retains its structure. The temperature of the entrance bump is lower on average due to its periodic deformation by the dense core. The flame is slightly shorter as shown in Figure 12 in the modulated case and the flame opening angle is more or less the same for the steady state and 1 kHz modulated cases.

DOI: 10.13009/EUCASS2022-4370

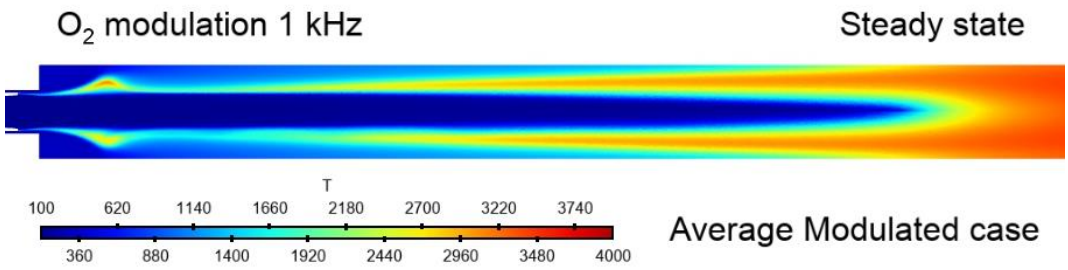

Figure 12: Comparison of the average temperature fields for the steady state (top) and the modulated case (bottom) at 1 kHz

The flame length is only slightly altered, but locally, the combustion zone widens and spreads due to the transverse movements of the flame and the wriklingding of the flame front.

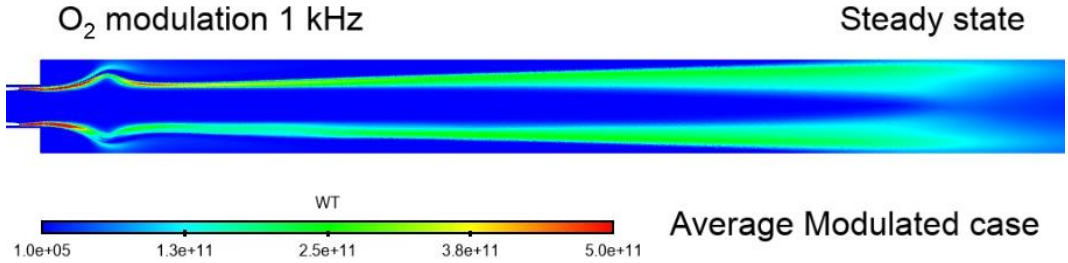

Figure 13 : Comparison of the average heat release fields for the steady state (top) and the modulated case (bottom) at 1 kHz

Figure 14 shows the time evolution of the temperature field over one period (T=1 ms) in the X=0 cross-sectional plane as well as the curve at the iso-value of the dense oxygen mass fraction $\left(Y_{O_2 dense} = 0.4\right)$. The deformation of the temperature input bump by the ripple propagating on the pseudo-interface of the dense jet is visible between t/T=0 and t/T=0.4.

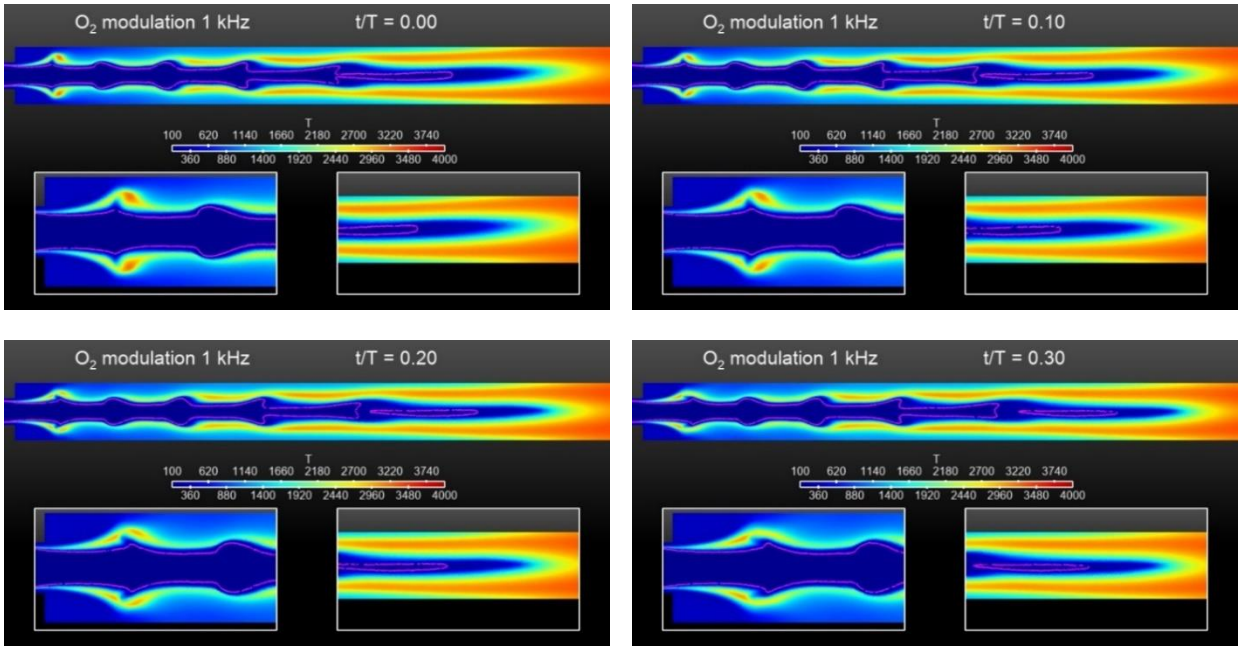

DOI: 10.13009/EUCASS2022-4370

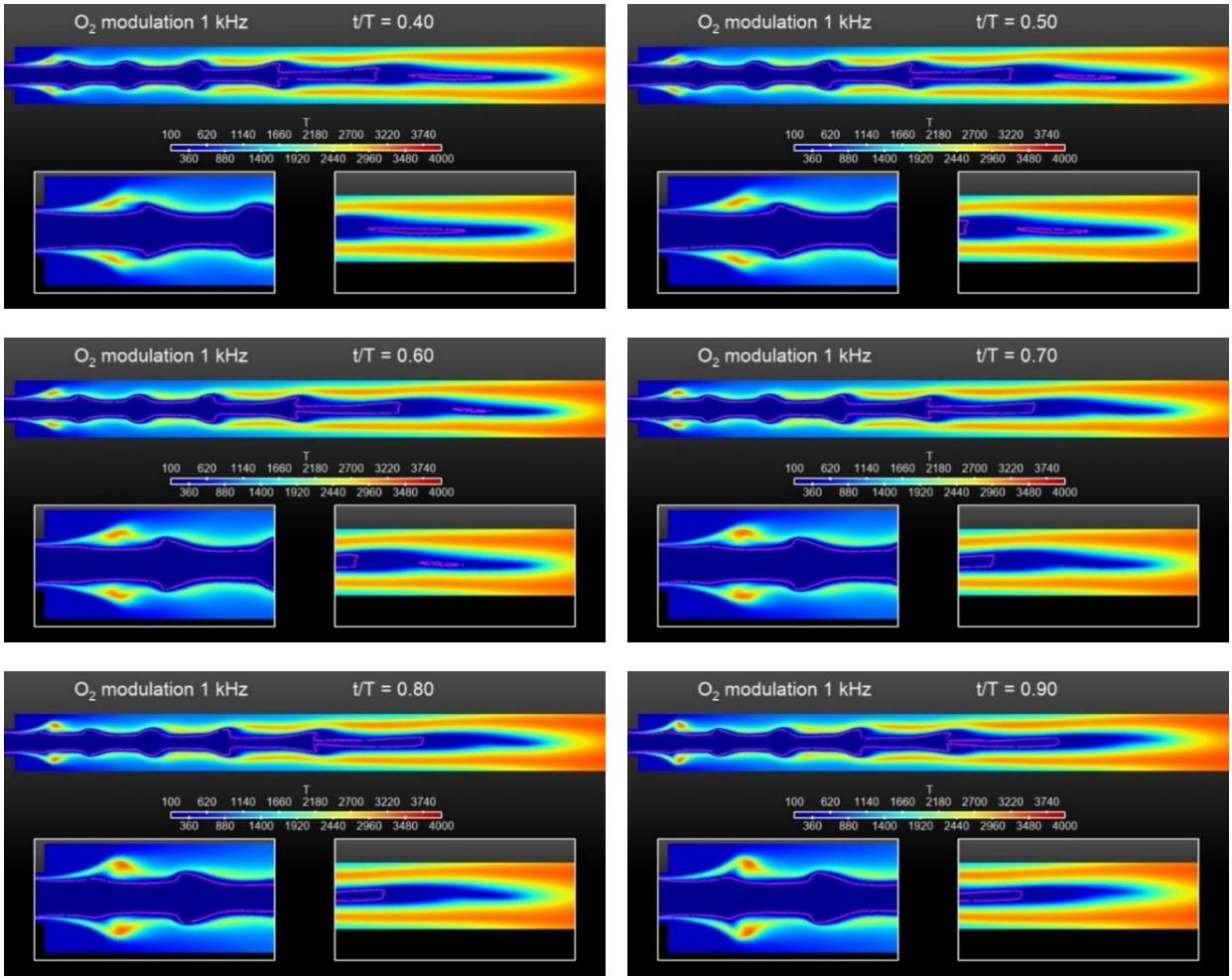

Figure 14: Temperature field in the X=0 plane with mass fraction iso-curve of O_2 dense ($Y_{O2dense}$=0.8) at 1 kHz

The cross-sections show the evolution of the dense jet which remains circular despite the undulation generated by the flow modulation (Figure 15). No asymmetry is apparent as shown in Figure 15. Thus, it shows the temperature field sections in the X=0 plane and in different cross-sections for six instants of a modulation period. An iso-curve of dense O_2 mass fraction at the value of 0.4 is also shown to represent the dense core. The dense core changes the position of the flame in the transverse planes but does not alter its circular shape.

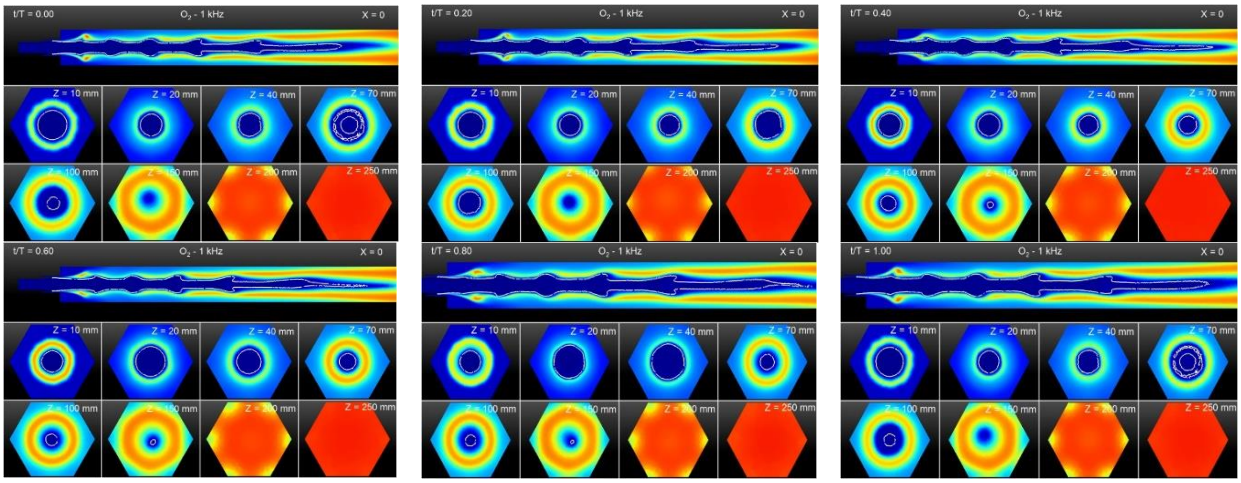

Figure 15 : Temperature field and iso-dense O_2 mass fraction (X=0 and cross sections) over one period for 1 kHz modulation

DOI: 10.13009/EUCASS2022-4370

5.2 Oxygen mass flow excitation at 5 kHz

When the oxygen line flow is excited at the 5 kHz frequency, structures similar to the 1 kHz case appear, but there are more of them, especially in the area near the injector. Their number corresponds well to the excitation frequency. Thus, every 0.2 ms, a ripple appears on the pseudo-interface of the dense core. Unlike the case at 1 kHz, this ripple appears at the injector lips. It then propagates over the pseudo-dense core surface. Moving away from the injection zone, the same arrow structure as in the 1 kHz case is found and the structures become less identifiable as they dissipate and the dense core breaks up, as shown in Figure 16a. Figure 16b gives the instantaneous streamlines together with a cross-section in the X=0 plane of the dense O_2 mass fraction. This figure shows a large inlet recirculation which constrains the dense jet, prevents the development of oscillations on the pseudo-interface and creates the inverted arrow shape.

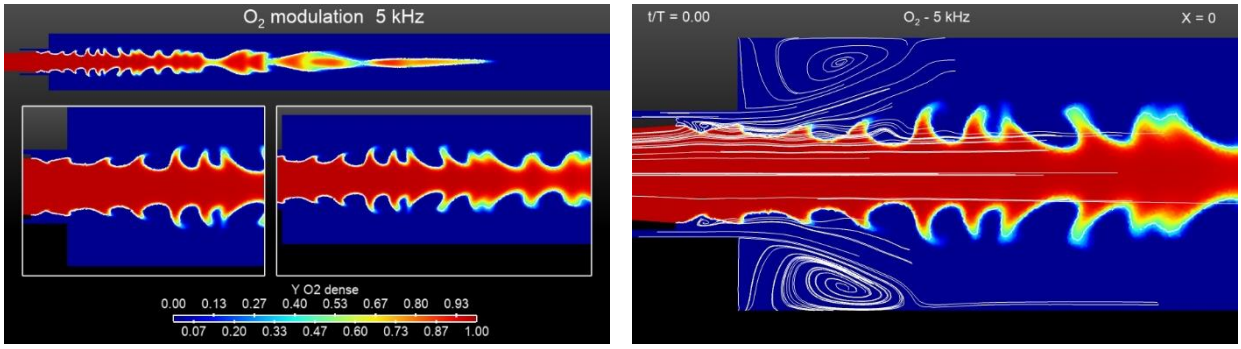

a) Different views of the dense jet b) Streamlines

Figure 16 : Deformation of the dense jet structure at 5 kHz

The structure of the dense jet is compared for the two modulation frequencies in Figure 17a. The 1 kHz modulated jet is shown in the upper half of the chamber and the 5 kHz jet in the lower half. The dense core is much more perturbed by the 5 kHz modulation and this leads to a greater shortening of its length. This is confirmed by the comparison of the mean fields. Indeed, the influence of O_2 flow modulation at 5 kHz is more important than for modulation at 1 kHz. The size of the liquid core is reduced by a factor of 2.5 instead of 2 (Figure 17b).

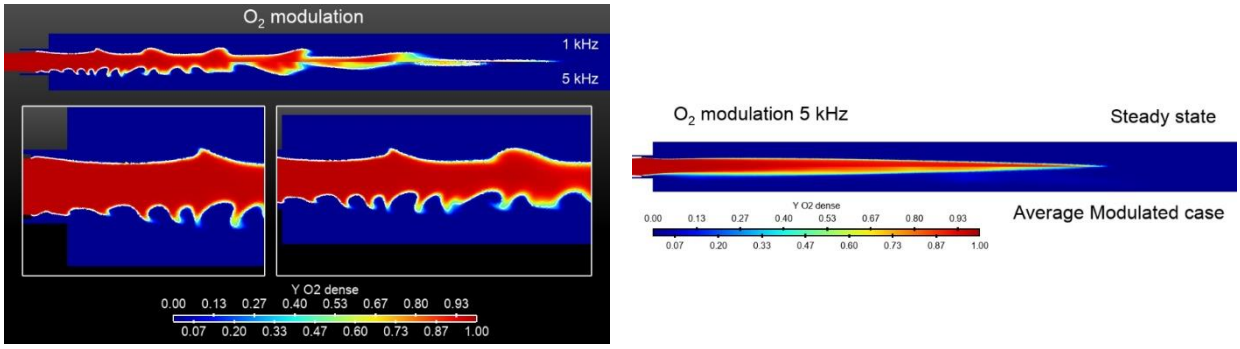

a) Instantaneous field b) Average field

Figure 17 : Comparison of the deformation of the dense jet structure at 5 kHz (bottom) and 1 kHz (top)

The flame is also 8% shorter as shown in Figure 18 and the shape of the injection bump is slightly different. The opening angle of the flame is not changed. The comparison between the two modulated cases shows that the flame is shorter and the liquid core more compact in the 5 kHz modulated case.

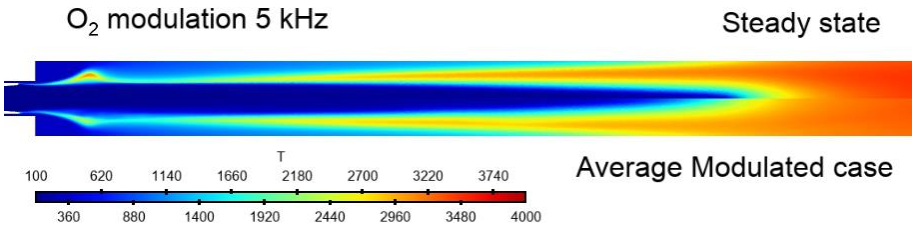

Figure 18: Comparison of the mean temperature fields for the steady state (top) and the modulated case (bottom) at 5 kHz

DOI: 10.13009/EUCASS2022-4370

In contrast to the case modulated at 1 kHz, the case at 5 kHz shows a change in the transverse circular structure of the dense core (Figure 19). The dense core remains circular near the injector and then starts to deform from Z=20 mm, taking on a square structure. The flame also deforms between Z=20 mm and Z=70 mm, changing from a circular shape to a square shape via a flower structure. After 100 mm, it returns to a circular shape.

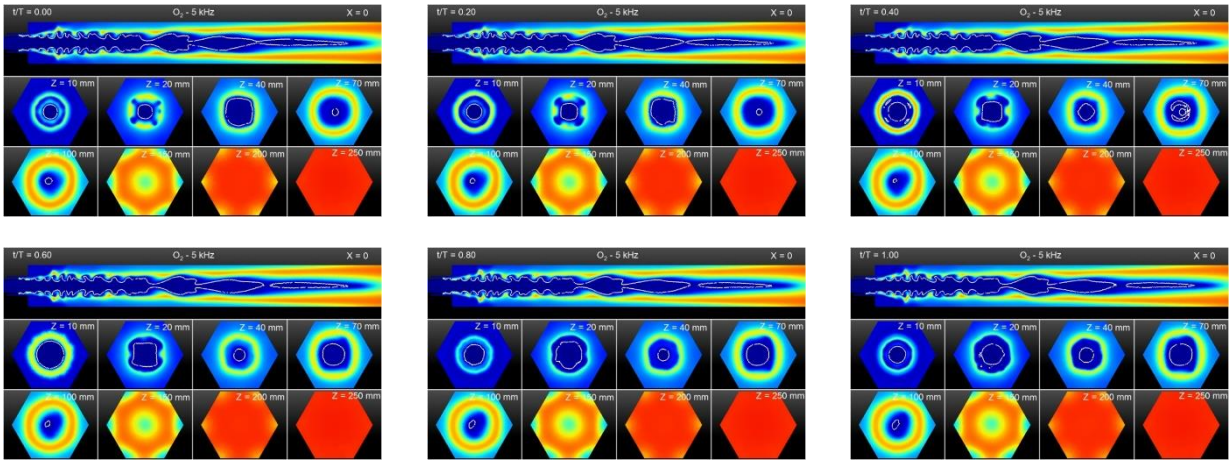

Figure 19 : Temperature field and iso-dense O_2 mass fraction (X=0 and cross sections) over one period for 5 kHz modulation

5.3 Methane mass flow excitation at 5 kHz

Only one modulation of the methane flow was performed, a modulation at 5 kHz. Ripples appear at the pseudo-interface of the dense core as with the oxygen flow modulations. However, these ripples have a smaller amplitude than those appearing with the O_2 modulations as shown in Figure 20. This figure represents the iso-value line of dense O_2 mass fraction for the three simulated modulations. White is the methane modulation at 5 kHz, green is the oxygen modulation at 1 kHz and purple is the oxygen excitation at 5 kHz. It is thus possible to compare the effect of the different modulations on the dense core. The latter is much shorter in the case of the O2 input modulation. The amplitudes of the ripples are of the order of 40% maximum for the methane modulation whereas they are 60% for the oxygen case. Moreover, the ripples attenuate much more rapidly in the case of methane modulation. Indeed, the ripples due to methane flow modulations disappear at about $5d_i$ while they continue until the end of the dense core for the case where the oxygen flow is modulated.

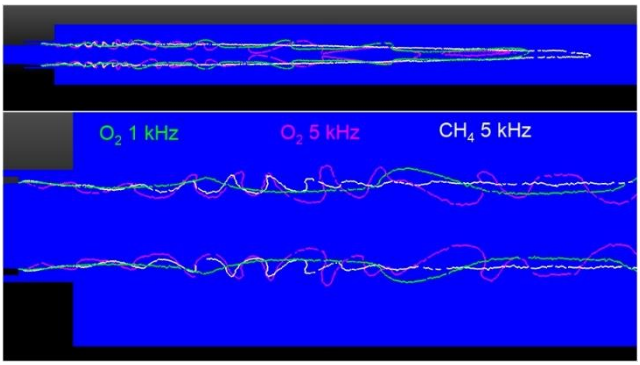

Figure 20 : Iso-curve of dense O_2 mass fraction (Y_{O2}=0.4) for the three modulated cases: CH_4 at 5 kHz (white), O_2 at 5 kHz (pink) and O_2 at 1 kHz (green)

To a lesser extent, the same structures appear on dense cores. These structures start at the lip of the injector with an inverted arrow shape (Figure 21). The structures are accelerated and eventually change shape to an outward pointing arrow at the bump of the temperature profile as confirmed in Figure 22.

DOI: 10.13009/EUCASS2022-4370

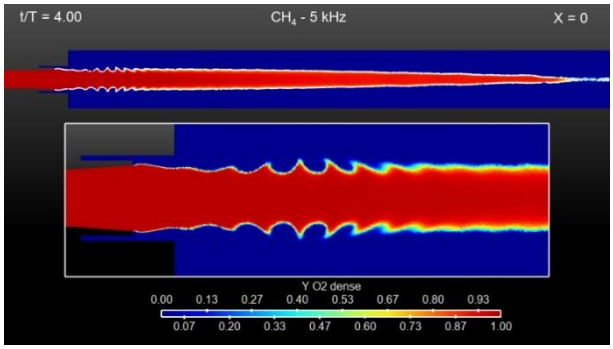

Figure 21 : Deformation of the dense jet structure by CH_4 flow modulation at 5 Hz

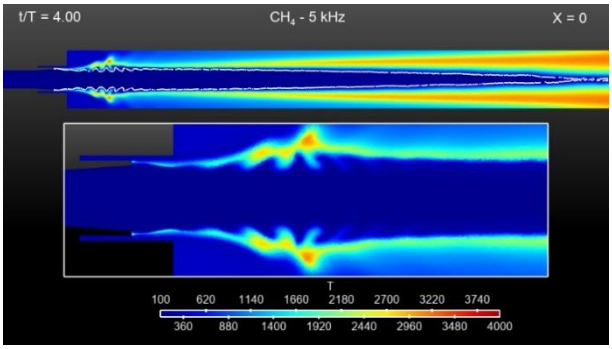

Figure 22: Instantaneous temperature field in the X=0 plane and mass fraction iso-curve YO2=0.4 in the case of CH4 flow modulation at 5 kHz

To further understand the phenomena altering the propagation of ripples at the pseudo-interface of the dense core, cross-sections of the axial velocity are plotted in Figure 23. This figure gives the time evolution of the velocity profile at z=0, z=5 mm, z=12 mm (corresponding to the temperature hump) and z =20 mm. The white curve represents the modulated case and the purple curve the steady state. The temperature field in the X=0 plane and the dense O_2 mass fraction iso-curve marking the dense core are also given in this figure. The maximum velocity reached by the methane jet represented by the two peaks in the sections oscillates around its mean value. At z=0, the peak variation amplitude is about 8% which is to be compared with the flow oscillations which are 10% and it decreases to 6% at z=5 mm. On the other hand, at the end of the recirculation at 12 mm, the amplitude at the peaks is of the order of 10% exacerbated by the counter-current that forms between the gas jet and the dense core. At z=20 mm, the flow modulation has almost no influence on the flow. It is recalled that the waves of the dense core pseudo-surface are no longer visible from Z=25 mm.

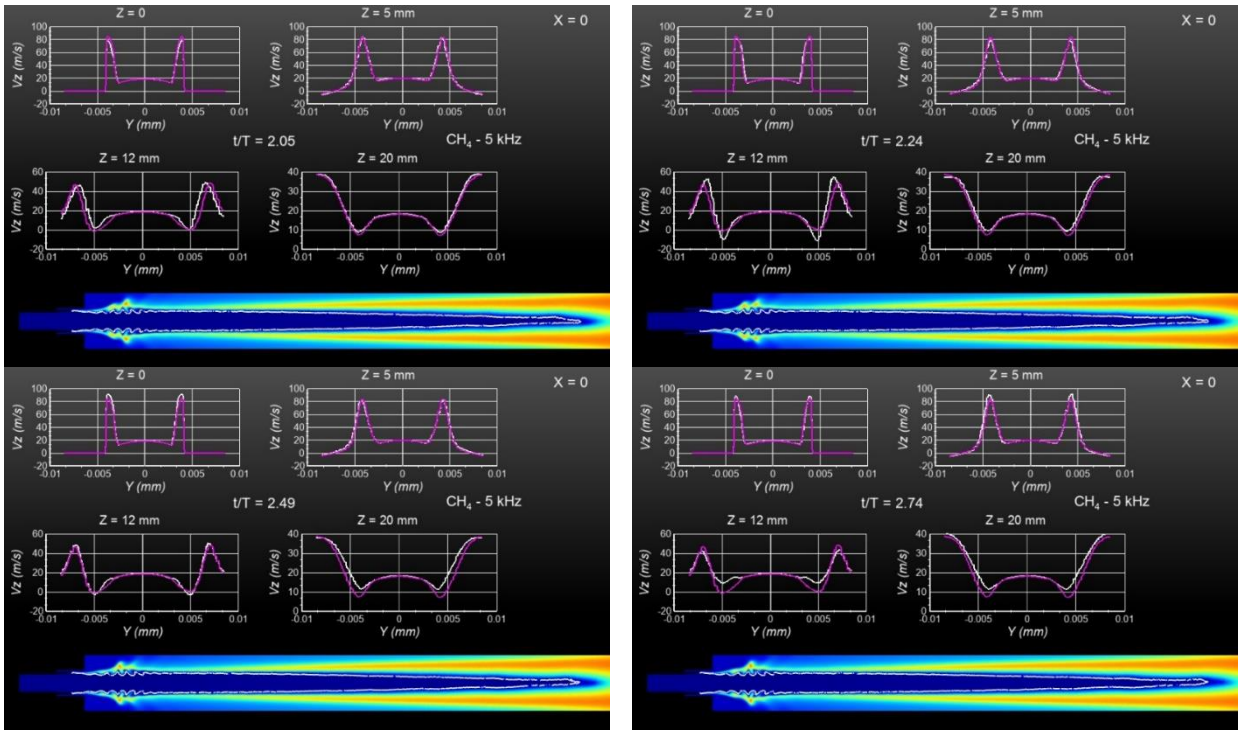

Figure 23 : Transverse velocity section at z=0, 5, 12 and 20 mm modulated case (white) and unmodulated case (purple)

The comparison of the average dense O_2 mass fraction fields (Figure 24) between the steady state (high half-chamber) and the average modulated case (low half-chamber) shows that the liquid core length is reduced by only 5% and the flame length is almost identical. As for the other cases, the temperature of the inlet hump that appears on the temperature field seems to be less important in the modulated case than in the stationary case. This is due to the fact that it is periodically distorted by the passage of the ripples on the dense oxygen pseudo-interface and the averaging operation attenuates its intensity.

DOI: 10.13009/EUCASS2022-4370

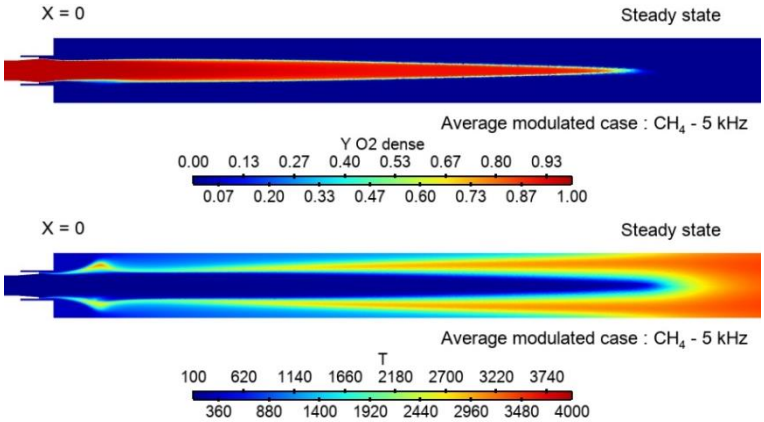

Figure 24 : Comparaison des champs moyens de température et de fraction massique de O2 dense pour le cas modulé en CH_4 à 5 kHz (bas) et l'état stationnaire (bas)

Finally, Figure 25 compares the evolution of the mean transverse temperature for the three modulated cases and the mean state. It confirms that the oxygen modulated case at 5 kHz has the most influence.

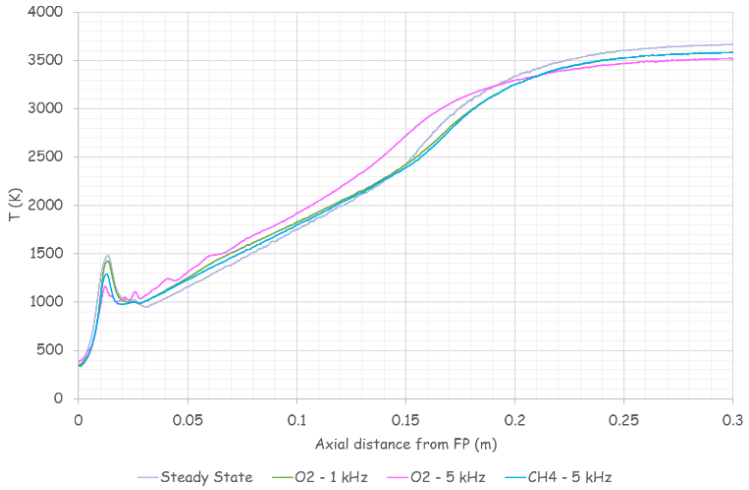

Figure 25 : Evolution of the average transverse temperature for the 3 modulated cases and the steady state

6 Conclusion

This study provided all the tools for the simulation of a cryogenic flame under supercritical injection conditions subject to flow oscillations. The calculations were successfully carried out with the U-RANS approach of the HF10 test case of the REST group modelling workshop. The effect of modulating the oxygen flow rate is greater than that of the methane flow rate and the 5 kHz frequency leads to a greater reduction in the length of the dense core than the 1 kHz frequency. The effect of the modulations is more important on the shape of the dense core than on the temperature field. To go further, the oxygen flow should be excited further upstream in the injection line with several frequencies at different amplitudes and study whether an eigenmode of the chamber-injection line system could be hooked as in the case of VHAM simulations and then lead to High Frequency combustion instabilities. Concerning the actual calculation of the HF10 case, the influence of the combustion model and turbulence as well as that of the thermodynamics of the species should be evaluated more precisely. Finally, an LES simulation of the same case should be carried out and compared with the U-RANS simulations.

7 References

[1] Sutton, G. P. and Biblarz, O. (2016). Rocket propulsion elements. John Wiley & Sons.
[2] Culick, F.E. (2006) Unsteady motions in combustion chambers for propulsion systems. AGARDograph, Technical Report, NATO/RTO-AG-AVT-039.

DOI: 10.13009/EUCASS2022-4370

[3] Anderson, W. and Yang, V. (1995). Overview of combustion instabilities in liquid-propellant rocket engines, liquid rocket engine combustion instability. Progress in Astronautics and Aeronautics, Vol 169, pp.3-37.
[4] Jensen R.J. et al. (1989) LOX/Hydrocarbon combustion instability investigation NASA contract NAS3-24612, NASA CR-182249, Rocketdyne
[5] Breisacher K., Priem R.J. (1990). Analysis of 5kHz combustion instabilities in 40K Methane/LOX combustion chambers. NASA TM 101368
[6] Refloch A., Courbet B., Murrone A., Villedieu P., Laurent C., Gilbank P., Troyes J., Tessé L., Chaineray G., Dargaud J.B., Quémerais E. and Vuillot F. (2011). CEDRE Software. Aerospace Lab, vol. 2.
[7] Menter, F. R. (1994). Two-Equation Eddy-Viscosity Turbulence Models for Engineering Applications. AIAA Journal. 32 (8): 1598–1605.
[8] A. Chemnitz, T. Sattelmayer, C. Roth, O. Haidn, Y. Daimon, R. Keller, P. Gerlinger, J. Zips and M. Pfitzner, (2018) Numerical Investigation of Reacting Flow in a Methane Rocket Combustor: Turbulence Modelling, Journal of Propulsion and Power 34: pp 864-877
[9] Le Touze, C., Murrone, A. and Guillard, H. (2014) Multislope MUSCL method for general unstructured meshes. Journal of Computational Physics RR-8463, pp.40.
[10] Toro, E.F., Spruce, M. and Speares, W. (1994). Restoration of the contact surface in the HLL-Riemann solver. Shock Waves, 4(1):25–34.
[11] Youcef Saad and Martin H. Schultz (1986) GMRES: A Generalized Minimal Residual Algorithm for Solving Nonsymmetric Linear Systems SIAM Journal on Scientific and Statistical Computing, Vol. 7, No. 3 : pp. 856-869
[12] Le Touze. C. (2015). Couplage entre modèles diphasiques à « phases séparées » et à « phase dispersée » pour la simulation de l'atomization primaire en combustion cryotechnique. PhD Thesis Université Nice Sophia Antipolis.
[13] Spalding, D. (1971). Mixing and chemical reaction in steady confined turbulent flames. Symposium International on Combustion 13:1 pp 649–657.
[14] Magnussen, B. and Hjertager, B. (1977). On mathematical modeling of turbulent combustion with special emphasis on soot formation and combustion. Symposium International on Combustion 16:1, pp 719–729.
[15] Schmitt, T. (2020). Large-Eddy Simulations of the Mascotte Test Cases Operating at Supercritical Pressure. Flow Turbulence Combust 105, 159–189.
[16] Goodwin, D.G. Speth, R.L. Moffat, H.K. and Weber, B.W. (2018) Cantera: An object-oriented software toolkit for chemical kinetics, thermodynamics, and transport processes.
[17] Gregory P. Smith, David M. Golden, Michael Frenklach, Nigel W. Moriarty, Boris Eiteneer, Mikhail Goldenberg, C. Thomas Bowman, Ronald K. Hanson, Soonho Song, William C. Gardiner, Jr., Vitali V. Lissianski, and Zhiwei Qin (1999) GRI 3.0 Mechanism. *Gas Research Institute (http://www. me. berkeley. edu/gri_mech)*.
[18] Giovangigli V. and Matuszewski L. (2012) Numerical simulation of transcritical strained laminar flames. Combustion and Flame, 159(9) pp2829-2840
[19] G.S. Soave (1972) Equilibrium Constants from a Modified Redlich-Kwong Equation of State. Chemical Engineering Science, 27, pp 1197-1203.
[20] Ely, J. F. And Hanley, H. J. M. "Prediction of transport properties. 1. Viscosity of fluids and mixtures" Industrial & Engineering Chemistry Fundamentals (1981) vol 20-4 pp 323-332 - American Chemical Society
[21] Gaillard, P., Giovangigli, V., and Matuszewski, L. (2016) A diffuse interface Lox/hydrogen transcritical flame model. Combustion Theory and Modelling 20 pp 486 - 520.
[22] Kim, T., Kim, Y., Kim, S. K. Real-fluid flamelet modeling for gaseous hydrogen/cryogenic liquid oxygen jet flames at supercritical pressure. Journal of Supercritical Fluids 58 (2011) 254– 262
[23] Nicole, A., Dorey, L.-H., Vingert, L., Theron, M. (2021) LES simulation for evaluation of acoustic response of subcritical coaxial flame submitted to High-Frequency acoustic fields Space Propulsion 2020+1